Supporting Information

Annealing experiments WS_2

As discussed in the main text, we initially performed annealing experiments on non-encapsulated monolayer WS_2. Figure S1 summarizes the results of these experiments. As shown in Figure S1(a), the emergence of a new emission peak in the PL spectra is observed starting from an annealing temperature of 1000 K. With increasing annealing temperature, the emission peak becomes progressively narrower. Figure S1(b) displays the narrowest emission peak obtained when scanning the sample, with a measured linewidth of 12 meV. In addition, power-dependent measurements reveal a clear saturation behavior of the emission intensity, which is characteristic of defect-related emission (Figure S1 (c)). These results demonstrate that thermal annealing successfully induces localized defect states in the WS_2 monolayer. The defect-related emission peak is located approximately 220 meV below the neutral exciton energy.
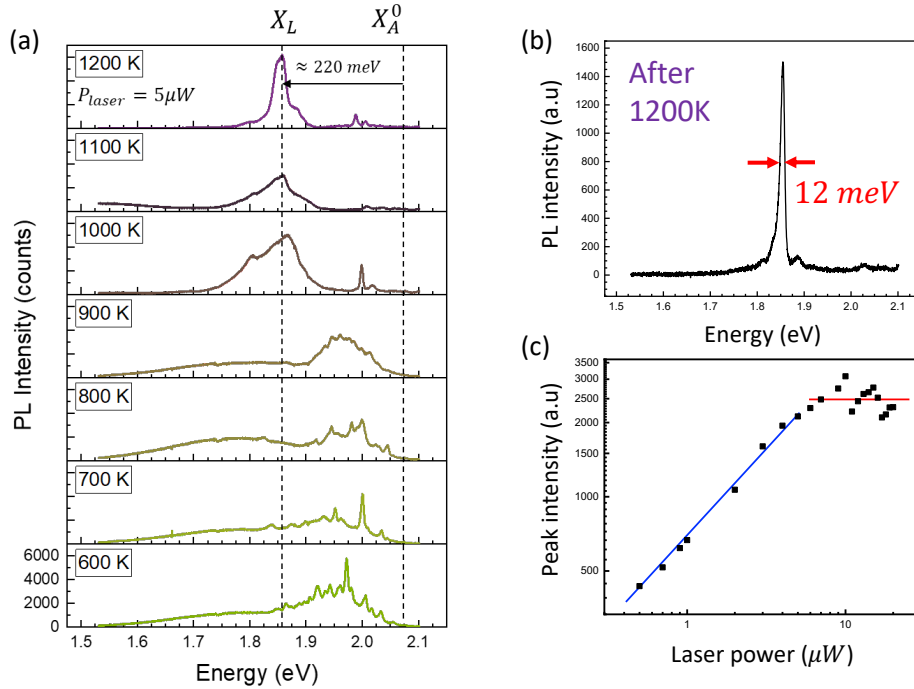

Figure S1: (a) Low-temperature ($T = 30$ K) PL spectra of non-encapsulated WS_2 monolayer measured after annealing at different temperatures . (b) Narrowest peak X_L in the PL spectrum obtained after annealing at 1200 K. (c) Power-dependent PL intensity of the XL peak measured using a CW laser ($\lambda_{\text{laser}} = 570$ nm).

The evolution of the PL spectra under thermal annealing was investigated in many other samples. Among them, this Figure S2 shows the emergence of narrow emission after 800K annealing. The PL spectra remain nearly unchanged up to 700 K; however, a new emission peak emerges at 800 K and becomes spectrally isolated after annealing at 900 K, as shown in Figure S2 (a) This emission line appears approximately 120 meV below the neutral exciton X_A^0, indicating a defect-related origin and suggesting that it likely corresponds to the same emission observed in non-encapsulated samples. The neutral exciton energy is more red-shifted at higher annealing temperature. The reduced energy separation with respect to the neutral exciton may be attributed to the well-known reduction of exciton binding energy in hBN-encapsulated monolayers, typically by about a factor of two. To further support this assignment, power-dependent PL measurements were performed on the newly emerging peak. As shown in Figure S2 (c), the emission intensity initially increases with excitation power and saturates above approximately 6 μW, which is a characteristic signature of emission from a finite density of localized defect states.
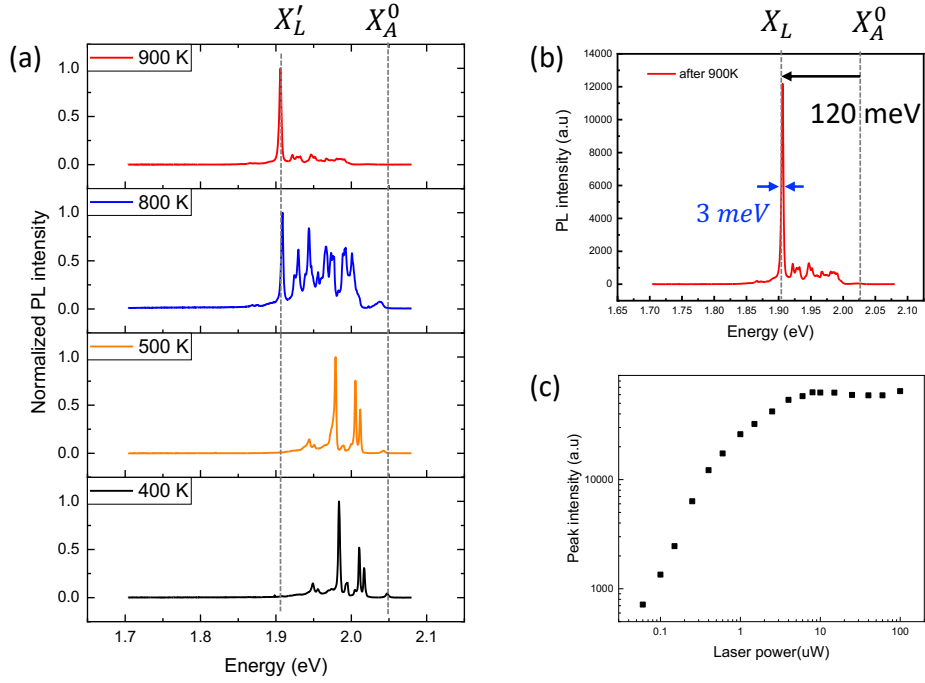
Figure S2: a) Low-temperature PL spectra of an hBN-encapsulated WS2 monolayer measured at $T = 3.6$ K after annealing at 400, 500, 800, and 900 K for 30 min. (λ_{laser} = 514.5 nm (CW), P_{laser} = 1 μW.) (b) PL spectrum recorded after annealing at 900 K, showing the emergence of a new narrow emission peak X_L located approximately 120 meV below the neutral exciton X_A^0. (c) Power-dependent PL intensity of the X_L peak.

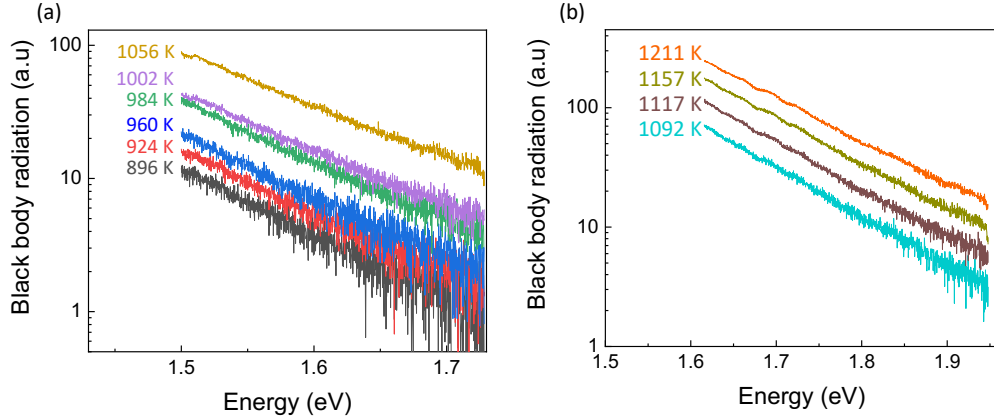## Extended temperature calibration using blackbody radiation

Figure S3: Blackbody radiation spectra of the suspended membrane used for extended temperature calibration at high temperatures. The spectra are fitted using Planck's law. (a)From 896 K to 1056 K, (b) from 1092 K to 1211 K

As shown in Figure **??**(a), the temperature is calibrated using the neutral exciton energy from 7.8 K up to 925 K. Figure S3 presents the blackbody radiation emitted by the membrane, which provides an extended

temperature calibration at elevated temperatures. The blackbody spectra are fitted using the second-order Planck's law:

$$B(\nu, T) = A(h\nu)^2 \frac{1}{e^{h\nu/kT} - 1}.$$

At 925 K, the temperature estimated from the blackbody radiation fit yields 924.4 ± 3.4 K, in excellent agreement with the exciton-based calibration obtained from Passler's model. For the remaining temperature points, the discrepancy between the two calibration methods remains within only a few kelvin.

Power-dependence measurements

In this section, we provide details on the saturation behavior observed in the power-dependent measurements shown in Figure **??**(b). A clear saturation of the PL peak intensity is observed as a function of excitation power. Since the excitation source is a pulsed laser, the PL intensity in the saturation regime can be expressed as

$$I_{PL}\,(\mathrm{s}^{-1}) = f_{rep}\,\Phi_y\,\eta_{opt}, \qquad \text{(saturation regime)}$$

where f_{rep} is the laser repetition rate, Φ_y is the quantum yield of the emitter, and η_{opt} is the optical collection efficiency. In the saturation regime, only one photon can be absorbed per laser pulse, as the emitter lifetime (0.9 ns) is much longer than the laser pulse duration (40 ps). Therefore, the PL intensity is simply given by the product of the laser repetition rate, the quantum yield, and the optical collection efficiency.

Outside the saturation regime, the probability that the emitter is excited during a laser pulse (P_{exc}) must be considered. The PL intensity can then be written as

$$I_{PL}\,(\mathrm{s}^{-1}) = P_{exc}\,f_{rep}\,\Phi_y\,\eta_{opt}.$$

If P_γ denotes the probability that a single photon excites the emitter, the excitation probability can be expressed as

$$P_{exc} = 1 - (1 - P_\gamma)^{N_\gamma},$$

which can be approximated as

$$P_{exc} \simeq 1 - e^{-N_\gamma P_\gamma}, \qquad \left[\lim_{N\to\infty}\left(1 + \frac{x}{N}\right)^N \approx e^x\right].$$

Experimentally, the power-dependent PL intensity can be fitted using the exponential form

$$I_{PL}(P_{avg}) \propto 1 - e^{-\frac{a}{f_{rep}}P_{avg}}.$$

By comparing the two expressions above, we obtain $P_\gamma = \alpha h\nu$. From the exponential fit shown in Figure **??**(b), $\alpha = 6.92 \times 10^{12}$ J^{-1}, which yields $P_\gamma = 2.73 \times 10^{-6}$ when multiplied by the photon energy $h\nu$.

The quantum yield Φ_y can be directly extracted in the saturation regime as

$$QY = \frac{R_{APD1} + R_{APD2}}{f_{rep}\,\eta_{opt}},$$

where R_{APD1} and R_{APD2} are the photon count rates detected by the two single-photon avalanche diodes (SPADs). Using a total detected count rate of 1000 counts/s and an optical collection efficiency of $\eta_{opt} = 2.44 \times 10^{-4}$—which accounts for losses in the objective, mirrors, beam splitter, filters, and coupling from the spectrometer to the SPADs—the resulting quantum yield is estimated to be **5.25%**.

Raman features of monolayer WS$_2$

Raman spectroscopy was performed on a pre-calibrated micro-membrane, as described in the main text. Figure S4 shows the evolution of the Raman spectra as a function of temperature from 25 °C to 1000 °C under vacuum conditions. Both the E_{2g} (in-plane vibrational mode) and A_{1g} (out-of-plane vibrational mode) peaks are observed in the Stokes region. In the anti-Stokes region, only the A_{1g} peak is detected, as the E_{2g} peak is suppressed by the notch filter.

With increasing temperature, the Raman peak intensities gradually decrease and eventually vanish at 1000 °C (1273 K), indicating that the WS$_2$ monolayer undergoes thermal degradation above this temperature. This result confirms that annealing can be safely performed at temperatures below 1000 °C.
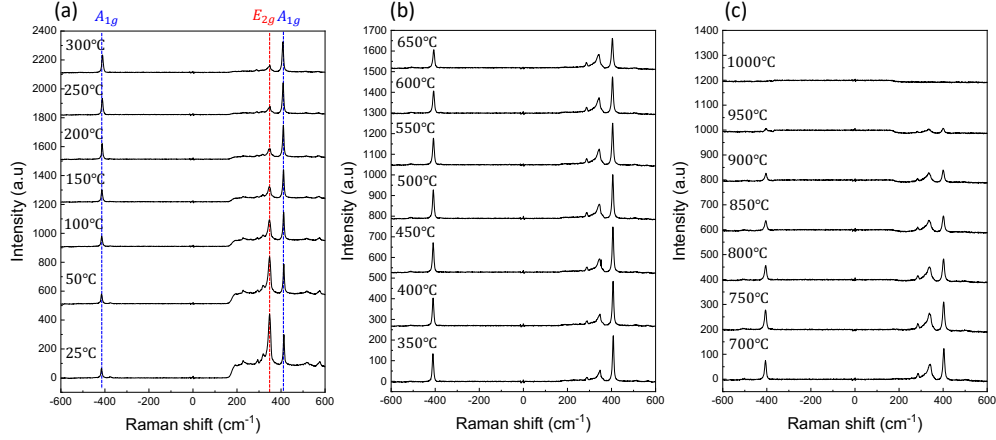

Figure S4: Temperature-dependent Raman spectra of monolayer WS$_2$ measured under vacuum. (a) Raman spectra recorded from 25 °C to 300 °C. (b) Raman spectra recorded from 350 °C to 650 °C. (c) Raman spectra recorded from 700 °C to 1000 °C. The E_{2g} and A_{1g} modes are observed in the Stokes region, while only the A_{1g} mode appears in the anti-Stokes region.

n addition to the intensity reduction, both Raman peak positions exhibit a redshift with increasing temperature. Figure S5 displays the temperature dependence of the A_{1g} mode in both the Stokes and anti-Stokes regions. A linear behavior is observed for both cases, with the Stokes A_{1g} mode showing a slope of -0.0139 cm^{-1}/°C. This value is comparable to previously reported results, where a linear fit of the Raman shift was obtained in the temperature range from 100 K to 600 K with a slope of approximately -0.0121 cm^{-1}/K [1]. The close agreement in slope confirms the consistency of our measurements, while the extended temperature range investigated here allows for a clearer assessment of the linear temperature dependence of the A_{1g} mode.
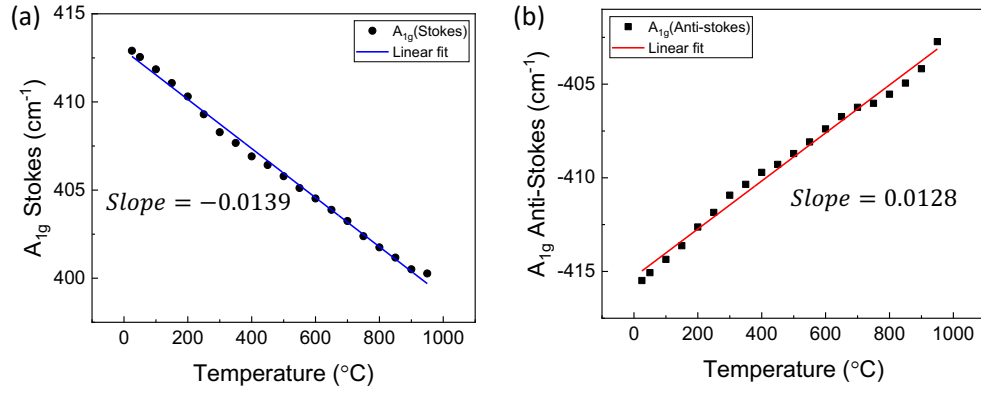
Figure S5: Temperature dependence of the A_{1g} Raman mode position in (a) the Stokes and (b) anti-Stokes regions, showing a linear redshift with increasing temperature.

References

(1)   Huang, X.; Gao, Y.; Yang, T.; Ren, W.; Cheng, H.-M.; Lai, T. *Scientific Reports* **2016**, *6*, 32236.